P6.1 VERIFICATION OF THE ORIGINS OF ROTATION IN TORNADOES EXPERIMENT, PART 2 (VORTEX2): DATA FROM THE NOAA (NSSL) X-BAND DUAL-POLARIZED RADAR

Christopher M. Schwarz[1,*] and Donald W. Burgess[2]
1. School of Meteorology, The University of Oklahoma, Norman, OK
2. Cooperative Institute for Mesoscale Meteorological Studies (CIMMS), The University of Oklahoma, Norman, OK

1. INTRODUCTION

The advantages of dual-polarimetric radar observations have been studied for some time (Zrnic and Ryzhkov 1999) and certain signatures have been found to exist in supercell thunderstorms. These signatures include the tornado debris signature (TDS; Ryzhkov et al. 2002, 2005a), the low-level Z_{DR} arc (e.g., Kumjian 2008; Kumjian and Ryzhkov 2008, 2008; Outinen and Teittinen 2007; Snyder 2008), Z_{DR} and K_{DP} columns (e.g., Caylor and Illingworth 1987; Illingworth et al. 1987; Tuttle et al. 1989; Meischner et al. 1991; Conway and Zrnic 1993; Brandes et al. 1995; Hubbert et al. 1998; Kennedy et al. 2001; Loney et al. 2002; Ryzhkov et al. 2005; Kumjian and Ryzhkov 2008), midlevel Z_{DR} and ρ_{HV} rings (Kumjian and Ryzhkov 2008; Kumjian 2008), updraft signature (Kumjian and Ryzhkov 2008), and hail signatures (Heinselman and Ryzhkov 2006). Each signature reveals a distinguishing distribution of hydrometeors. Varying hypotheses have correlated these characteristics to different kinematic properties of the parent storm and its interaction with the environmental flow.

Most dual-polarimetric studies have been performed at S- and C-bands (e.g., Kumjian and Ryzhkov 2008, Romine et al. 2008, Ryzhkov et al. 2005a, Ryzhkov et al. 2002, Van Den Broeke 2008), but relatively few studies have been made at X-band. Snyder (2008) examines X-band dual-polarimetric observations from UMass X-Pol using different cases for different estimates of attenuation and differential attenuation in order to mitigate the impacts of both. Among his findings (see the paper for more details) is that the correction technique called the ZPHI-Rain Profiling Algorithm (Testud et al. 2000) performs amongst the best of all the tested cases. The techniqued is used in results presented in this paper. Some details and limitations of the algorithm will be briefly described as well.

The main focus of this paper is to provide a summarized analysis of storm evolution obtained from the NOAA (NSSL) X-Band Polarized (NOXP) mobile weather radar during the **V**erification of the **O**rigins of **R**otation in **T**ornadoes **EX**periment, Part 2 (VORTEX2) field project. Herein the hail signature, Z_{DR} arc, and Z_{DR} and K_{DP} column signature evolution are analyzed in

correspondence to the evolution of the updraft signature from two supercells, one significantly tornadic (June 5, 2009) and one weakly tornadic (June 7, 2009). This paper gives a general overview of the observations and evolution seen at X-band (3-cm) wavelength.

2. METHODOLOGY

2.1. *Data Collection*

For eleven and ½ weeks NOXP collected data during the VORTEX2 field campaign. NOXP collected data as a mesocyclone-scale radar (a radar assigned to scan the low- to mid-level regions of the storm at relatively close range (5-30 km)). It provided dual-polarimetric observations and dual-doppler with other mesocyclone scale radars (two Doppler on Wheels: DOW6 and DOW7) and UMass X-Pol. Table 1 details NOXP specs for 2009. The advantage of this mobile radar is high spatial resolution and fast updates. During both days, NOXP performed two-minute time syncs, and scanning strategies are listed in Table 1.

Name	NOXP
Type	X-Band ($\lambda \approx 3.21$ cm)
Frequency	9410 MHz
3-dB Beamwidth	1.0°
Effective Beamwidth	~1.45°
Azimuthal Sampling Rate	1.0°
Antenna Rotation Rate	**Low Resolution:** 28° sec^{-1} **High Resolution:** 29° sec^{-1}
Peak Power	250 kW
Processor	Sigmet RPV8
Pulse Repetition Frequency (PRF) /Nyquist Co-Interval	**Low Resolution:** ~950 Hz / +/- 7.6 m/s **High Resolution:** ~1700 Hz/ +/- 13.6 m/s
Gate Spacing	**Low Resolution:** 150 meter **High Resolution:** 75 meter
Max Unambiguous Range	**Low Resolution:** 158 km **High Resolution:** 88 km
Number of Samples	**Low Resolution:** 32 **High Resolution:** 60
Scanning Strategy (Elevations collected)	**Low Resolution:** 0.5°-8.5° (1° interval) **High Resolution:** 0.5°, 1.0°-11.0° (1° interval)

Table 1 – Specifications for the NOXP mobile weather radar during the 2009 data collection

* *Corresponding author address:* Christopher Schwarz, University of Oklahoma, School of Meteorology, 120 David L. Boren Blvd., Rm. 4340D Norman, OK 73072-7307; email: cmschwarz@ou.edu

Low Resolution (low PRF) data were collected initially for both data sets, and shortly thereafter High Resolution (high PRF) data were collected for the remainder of the deployment. Low Resolution velocity data were deemed unrecoverable due to the low Nyquist co-interval.

2.2. *Data Preparation*

The NOXP data from the June 5 and June 7 storms were first de-cluttered and de-aliased (if possible) using Solo II (Oye et al. 1995) and heading corrections were performed. The data were converted from DORADE Sweep files to NetCDF format using the Foray translator developed by Dennis Flannigan at the National Center for Atmospheric Research (NCAR). Attenuation corrections are made using the ZPHI method in a program written by Jeff Snyder for work in Snyder (2008). The program calculates the propagation differential phase (ϕ_{DP}) by filtering and smoothing the measured total differential phase (Φ_{DP}) using a smoothing depth of 2 km. This is based on iterative filtering developed by Hubbert and Bringi (1995). Then attenuation and differential attenuation are calculated and applied to the reflectivity factor (Z_H) and differential reflectivity factor (Z_{DR}) fields. For more information about the program, the reader is deferred to Snyder (2008). Factors affecting the technique are discussed in Section 3.

A 3-Dimensional Barnes 2-pass objective analysis scheme (Barnes 1964; Koch et al. 1983; Majcen et al. 2008) was implemented for the moment and polarization data for each case. The weighting function for the Barnes objective analysis scheme uses a Gaussian distribution of weights (Barnes 1964). κ_0 is assigned equal values in all three dimensions, and is calculated using the recommended calculation from Pauley and Woo (1990) using the coarsest data separation in the data set. $\kappa_0 = 0.450$ for June 5, $\kappa_0 = 0.121$ and $\kappa_0 = 0.215$ for June 7. A constant γ value of 0.3 was used for every case after examining response functions as detailed in Majcen et al. (2008). More than one set of values is used for June 7 due to changing proximity to the radar. Grid points and grid spacing values were chosen for computation optimization and scale of features. Storm propagation was not accounted for in the objective analysis.

Constant Altitude Plan Position Indicators (CAPPIs), Range Height Indicators (RHIs), and vertical cross-sections were obtained using the *Vis5d* (ftp://ftp.ssec.wisc.edu/pub/vis5d-5.2/README) visualization software. All height calculations in the objective analysis are calculated using equation 2.28b from Doviak and Zrnic (1993) (i.e. the 4/3's earth's radius rule).

3. HYDROMETEOR IMPACTS ON SIGNAL

3.1. *Attenuation: A_H and A_{DP}*

One of the most useful measures from Doppler radar is reflectivity factor $Z_{H,V}$. However, at shorter wavelengths (such as X-band), $Z_{H,V}$ is more prone to signal loss, or attenuation. Attenuation is more prevalent when hydrometeor size diameters become comparable to radar wavelength. Hydrometeor type, number concentration, and distribution within the resolution volume all contribute to attenuation. Significant attenuation (A_H and A_V) (subscripts H and V denote the horizontally and vertically polarized waves) is more likely to occur with interactions of liquid hydrometeors rather than ice hydrometeors owing to the much higher dielectric factor of water. Unattenuated reflectivity factor $Z'_{H,V}$ (dBZ) can be obtained by simply adding the two-way path integrated attenuation $PIA_{H,V}$ (dBZ km^{-1}) (Bringi and Chandrasekar 2001) down a radial to the measured $Z_{H,V.}$

Differential reflectivity factor Z_{DR} also suffers from attenuation. If the horizontal wave attenuates more than the vertical wave, or vice versa, this is referred to as specific differential attenuation (A_{DP}) and is given by: $A_{DP}=A_H-A_V$. A measure of the unattenuated differential reflectivity factor (Z'_{DR}) is obtained by adding the two-way path integrated *differential attenuation* PIA_{DP} (dB km^{-1}) (Bringi and Chandrasekar 2001) down a radial to the measured Z_{DR}. Differential phase data (both specific (K_{DP}: e.g. Bringi et al.1990; Park et al. 2005) and ϕ_{DP}: (Testud et al. 2000; Ryzhkov and Zrnic 1995; Bringi et al. 2001)) have been tested in different relationships to mitigate A_H and A_{DP}. K_{DP} is simply the range derivative of ϕ_{DP}. However, K_{DP} tends to be noisy in the presence of resonance scatterers i.e. backscatter differential phase (δ).
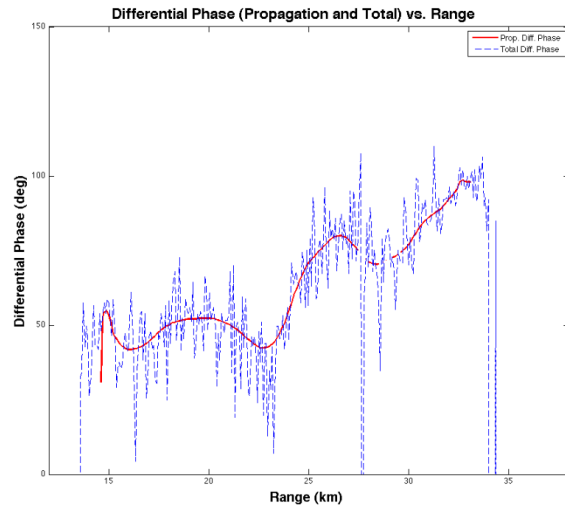

Figure 1 – Total differential phase (Φ_{DP}) and extracted propagation differential phase (ϕ_{DP}) vs. range. Data are taken from the 299.74° azimuth on June 7, 2009. ϕ_{DP} is obtained using a triangular weight function with a smoothing depth of 2 km.

Extraction of accurate ϕ_{DP} from Φ_{DP} (related as: $\Phi_{DP} = \phi_{DP} + \delta$ (Bringi and Chandrasekar 2001)) requires removal of δ as it contributes to large Φ_{DP} initially or at the end of an echo down a radial. Figure 1 shows measured Φ_{DP} and the retrieved **ϕ_{DP}** with respect to range for the 299.74° radial on June 7, 2009. The iterative method works as long as there is no significant δ at either edge of the echo that spans greater than 2 km. Thus removal of δ is not always possible, but "buffers" in the program help to mitigate this. As noted in Snyder (2008) the expense is the removal of data.

3.2. *ZPHI correction*

The ZPHI algorithm (Testud et al. (2000)) constrains path-integrated attenuation by the total change in ϕ_{DP} along a radial through a rain cell. Assuming a pure rain medium induces some errors into the approximations for attenuation and differential attenuation. Hail presents a challenge for attenuation estimates, as the fractional water content determines the amount of significant attenuation. This technique requires the exponent (*b*) in the $A_H - Z_H$ relation as defined in Hitschfeld and Bordan (1954). Temperature and drop shape variation have little effect on *b*. Another required coefficient is α_H in the $A_H - K_{DP}$ relation (Bringi et al. 1990; Jameson 1992; Park et al. 2005a). α_H varies greatly as a function of the DSD, temperature, and drop shape relation. Different studies using disdrometer data have found varying values for α_H for X-Band (e.g. Bringi et al. 1990; Matrosov et al. 2002; Jameson 1991; Zhang 2008 (*personal communication*); Park et al. 2005a). A constant value of $\alpha_H = 0.32$ and a value of b = 0.722 were chosen for the corrections used in this study, however holding α_H constant is not a good assumption in areas of large raindrops (Ryzhkov and Zrnic 2005).

In regions of total attenuation the ZPHI technique does not work, as there is no change in ϕ_{DP} down the radial. Hitschfeld and Bordan (1954) find $A_{H,V}(r)$ at all locations between *r* and r_0 may be calculated by

$$A_{H,V}(r) = \frac{Z_{H,V}^b(r)\{10^{0.1ba\Delta\phi_{DP}} - 1\}}{I(r,r_0) + \{10^{0.1ba\Delta\phi_{DP}} - 1\}I(r,r_0)} \quad (1)$$

where the *I* (Testud et al. 2000) is the path integral down a ray, *r* is the beginning range of the ray, r_0 is the ending range of the cell, and where $\Delta\phi_{DP} = \phi_{DP}(r_1) - \phi_{DP}(r_0)$.

The ZPHI algorithm allows for the estimation of the normalized slope parameter N_0^* (see the paper for more details) down a radial, which is then related to A_{DP} as

$$A_{DP} = p[N_0^*]^{1-q} A_H^q \quad (2)$$

where $p \approx 4.38$ and $q \approx 1.224$ at X-band, after which time Z_{DR} can be corrected (Snyder 2008). Correcting differential reflectivity using this algorithm was found to underestimate A_{DP} when compared to other correction techniques. The coefficients are believed to be to small, and this is currently being investigated (Snyder 2008).

3.3. RESONANCE IMPACTS

Resonance (Mie) scattering occurs for different diameters of differing hydrometeor type, and increases for shorter wavelengths. Barring the impacts of attenuation, resonance impacts cause an oscillation in the amount of backscatter signal that the radar receives. However, resonance at X-band is less than C-band due to increased attenuation. These fluctuations impact $Z_{H,V}$, Z_{DR}, K_{DP}, and the co-polar cross-correlation coefficient at zero lag $|\rho_{HV}(0)|$, or simply ρ_{HV}. Since $Z_{H,V}$ and Z_{DR} are a measure of the returned signal, their measurements oscillate as well. δ increases in the presence of resonance scattering, which can directly lead to highly negative K_{DP} values, and ρ_{HV} naturally is lower than 1.0 in a pure rain regime. For very large hydrometeors, ρ_{HV} can yield very low values.

Rayleigh scattering occurs for diameters D < $\lambda/16$, or more accurately by D=$(\lambda\mathfrak{R})/(|\varepsilon|)^{1/2}$ (Kumjian 2008; Kumjian et al. 2008) where $\mathfrak{R} \approx$ 1.0, 1.5, 2.0, 2.5, etc. As $\mathfrak{R}$ increases the impacts decrease due to increasing attenuation (Kumjian 2008). For X-band, resonance scattering occurs around ~1 mm sized raindrops. Since hail is larger than 1 mm, all sizes reside in the resonance regime. Differing dielectric properties of water and ice yield different fluctuations of scattering. The fractional water content of an ice hydrometeor will impact the amount of returned signal, but an increase in liquid water on the ice hydrometeor will increase the attenuation that has a dampening effect on resonance scattering (Snyder 2008). Fluctuations of the dielectric constant for varying temperature of the propagation medium tend to fluctuate the amount of resonance scattering that occurs (Ryzhkov and Zrnic 2005).

4. 5 JUNE 2009

On June 5, 2009 the VORTEX2 armada intercepted a tornadic supercell in Goshen County, Wyoming. The tornado developed at ~21:55 UTC as NOXP was in transit to a deployment spot. Data collection began with low-resolution scan at 22:16:09 UTC around the peak intensity of the tornado, which will be discussed briefly in the next section. High-resolution data began collection at 22:22:17 and ended at 22:43:47 UTC. Local soundings indicate that the environmental melting level is ~4.25 km above sea level. The in-cloud melting layer, away from the updraft region is observed to be ~3.1 km above sea level.

4.1. *Tornado Debris Signature*

At 22:16:09 UTC, the tornado is seen as a Z_H depression (a minimum of ~30 dBZ) at 0.25 km in height in the location of the tornadic vortex signature (TVS) as seen in Figure 1 below.
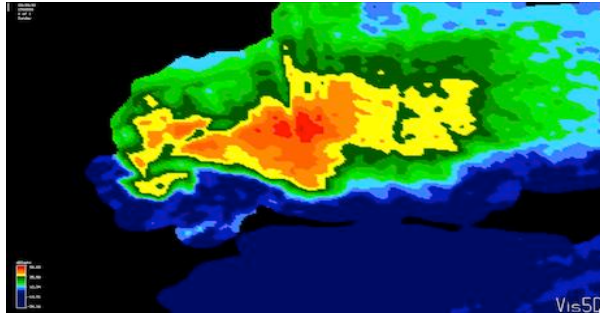

Figure 2 - CAPPI at 0.25 km in height illustrating the TVS signature in Z_H. This signature is associated with the centrifuging of hydrometeors (Dowell et al. 2005).

Values between ~51 to ~57 dBZ surround the tornado's location above ~1.0 km. The tornado was rain-wrapped initially, but was more visible by this time. The larger reflectivity values are thought to be associated with the tornado debris signature (TDS). The TDS is hard to discern as ρ_{HV} drops out in the location of the TVS, and Z_{DR} reduces slightly to ~2.0 dB. Perhaps ρ_{HV} is dropping out from noise caused by randomly oriented debris? The poor resolution of this signature makes it difficult to determine. The signature is not as well defined at 22:17:55 UTC, and the low-level circulation begins to weaken at 22:26:17 UTC. The velocity couplet disappears at ~22:30:21 UTC coinciding with the full dissipation of the tornado, but a remnant region of weak shear remains.

4.2. *Updraft Signature*

As noted before in previous literature updraft signatures are characterized by a reduction of ρ_{HV}, a collocated Z_H reduction region, and a flanking Z_{DR} column. Ryzhkov et al. (2005) and Kumjian (2008) speculate that the lower value of ρ_{HV} may be an indirect measure of updraft strength, but dual-Doppler analyses and vertical velocity retrievals are necessary but not available to prove the hypothesis. These reductions have been attributed to variable factors such as light debris (dust, insects, grass, leaves, etc.) caught in inflow at lower-levels. Aloft, possibilities include sparse large irregularly shaped hail, tumbling hail, mixed unfrozen and frozen particles, or a low number concentration of hydrometeors (Kumjian 2008; Kumjian et al. 2010), which will substantially reduce ρ_{HV}. Without dual-Doppler wind retrievals there is no definitive evidence to suggest that the sequence of updrafts that will be presented are the dominant updrafts. What is actually

believed to be occurring is a sequence of pulses in updrafts, which will be discussed more thoroughly.

During the volume scan at 22:16:09 UTC, there appears to be two updraft pulse regions. This is inferred from the two bounded weak echo (BWER) regions as seen in Figure 3. Updraft 'A' is located on the eastern flank of the hook, updraft 'B' is located due east of A, and 'C' which is first seen at 22:18:55 UTC, is to the southeast of B. A is believed to be the parent updraft, associated with the WER region, B is believed to be forced by the advancing rear-flank gust front, and C is also believed to be forced by the rear-flank gust front but more on the leading edge.
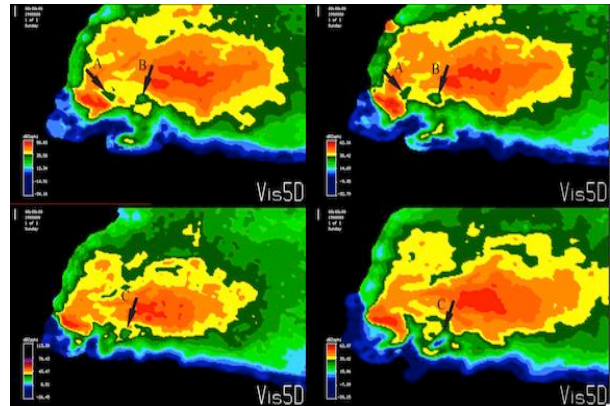

Figure 3 - Updraft A, updraft B, and Updraft C. CAPPI 1 (upper left) taken at 22:16:09 UTC at 4.09 km, CAPPI 2 (upper right) taken at 22:17:37 UTC at 3.50 km, CAPPI 3 (lower left) taken at 22:18:55 UTC at 4.49 km, and CAPPI 4 (lower right) taken at 22:20:24 UTC at 4.15 km.

The height of the BWER is often considered a measure of updraft strength. Examining the four times in Fig. 3, A's BWER diminishes above 5.50 km, whereas B's BWER is seen to the top of the volume. At 22:17:37 UTC the strength of both A & B diminishes as the height of the BWER is last seen at 4.15 km. C develops at 22:18:55 UTC and increases in intensity as the top of the BWER is not seen at 22:20:24 UTC. Examining the same regions with ρ_{HV}, one can identify roughly the same locations as updraft. The reduction of ρ_{HV} is dependent on the number concentration and particle type, i.e. SNR biases ρ_{HV} in a BWER without scatterers. CAPPIs of ρ_{HV} taken at the same altitudes and times (Figure 4) indicate updraft locations. Using these reductions regions, one could deduce the "source" regions of particles for a given wind pattern within the storm. However, one must also consider the possibility of vertical trajectories, such as descending ice hydrometeors or supercooled liquid drops advecting within and exiting the updraft.

The horizontal extents of anomalously low ρ_{HV} seen in Figure 4 are more often characterized by extremely variable values of Z_{DR} (-0.6 -~3.5 dB), and Z_H values between ~30 to ~43 dBZ. The lowest reduction near the updraft could be the result of large irregularly shaped or tumbling hail, whereas the region farthest

from the updraft center could be advection of graupel around the north side of the updraft. Intense updrafts have more intense divergence signatures aloft, which can carry smaller particles with lower terminal
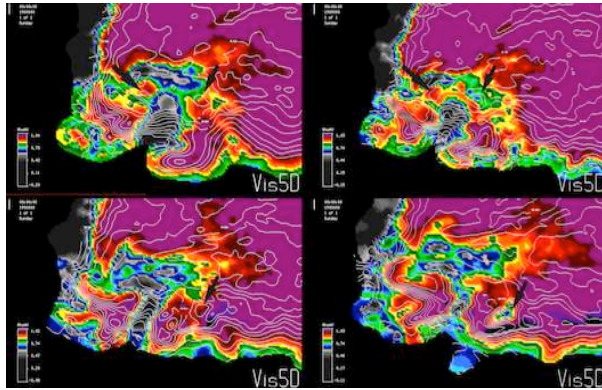

Figure 4 - CAPPIs are taken from the same times and same heights as in Figure 3. White contours are Z_H every 5 dBZ. Arrows indicate the location of the BWERs presented in Figure 3. Note that the lower ρ_{HV} regions flank and coincide with the location of the updraft.

velocities farther. This could explain these reduction regions. Furthermore, it should be noted that Z_{DR} is biased by noise down radial from the hook region as seen in regions of strong A_H and A_{DP}. Optimal SNR values for adequate ρ_{HV} measurements at X-band are still being investigated.

At 22:26:04 UTC, updraft 'D' is seen both in Z_H, Z_{DR}, and ρ_{HV} from CAPPIs in Figure 5 taken from multiple heights at this time. The presence of a very broad BWER at C's location still indicates that updraft C is present.
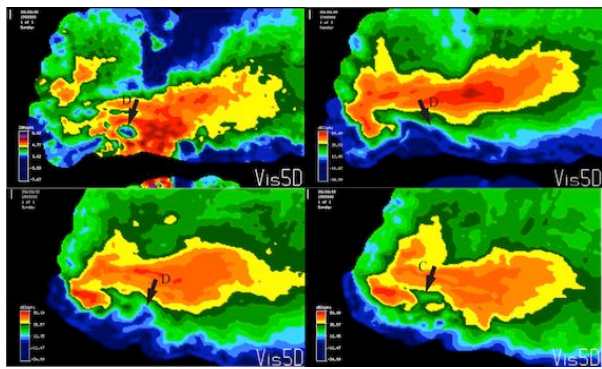
Figure 5 - 22:26:04 UTC CAPPIs of Z_{DR} (upper left) at 0.79 km, Z_H (upper right) at 0.79 km, Z_H (lower left) at 3.75 km, and Z_H (lower right) at 5.11 km. Updraft 'C' coincides with the broad BWER, but the Z_H reduction and WER region at 3.75 km coincides with updraft 'D'.

Examining the height of the BWER, and the significant reduction in Z_{DR} at 0.79 km associated with D, one can infer the presence of a strong updraft. Between 22:30:05 and 22:32:04 a new updraft pulse 'E' is seen, which is slightly south of updraft D as shown in

the CAPPIs taken at 4.69 km in Figure 6. Anomalously low values of ρ_{HV} (< 0.4) extend around the northern flank of the gust front as seen in Figure 6. Given the low Z_H values, one can infer low number concentration in the sampling volume. Low SNR bias is likely responsible for these reductions. The updraft signature is more vigorous at 22:34:04 UTC (not shown). The Z_{DR} values between ~-0.6 to ~1.5 dB, and varying ρ_{HV} between ~0.75 to ~0.84 at low-levels (~0.25 to ~0.4 aloft). The reduction region extends around in a cyclonic fashion marking a narrow region of low Z_H, low ρ_{HV}, and low Z_{DR}.
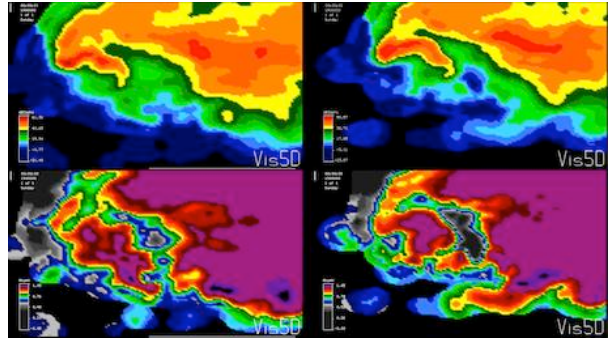

Figure 6 – CAPPIs at 4.69 km of Z_H (top) and ρ_{HV} (bottom), which are taken from 22:30:05 UTC (left) and 22:32:05 UTC (right). The development of updraft 'E' is seen at 22:32:05 UTC.

Between ~22:36:00 UTC and ~22:37:00 UTC an increase in Z_H (now up to ~43 dBZ), ρ_{HV}, and low-level Z_{DR} marks an increase in precipitation in the WER at low-levels. Echo associated with the gust front has reached the southern edge of the forward flank. The increase in hydrometeors at this height has increased Z_H and ρ_{HV}. At 22:38:04 UTC a new updraft pulse is seen on the southern edge of updraft D. This updraft, which is referred to as updraft 'E', is seen in Figure 7 below. Also shown south of E is updraft pulse 'F'.
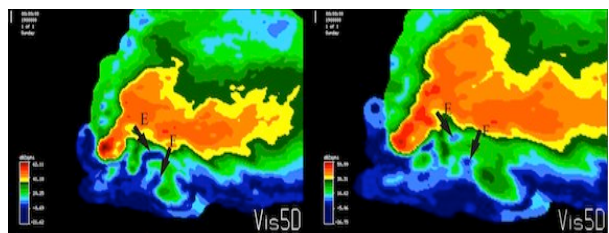

Figure 7 - CAPPIs of Z_H from 2.36 km in height at 22:38:04 UTC (left) and 23:40:02 UTC (right). The location of updraft 'E', and the new updraft 'F' are identified with arrows.

There is an increase in the amount of precipitation (i.e. increase in Z_H) in updraft E's region at 22:40:02 UTC (Figure 7) indicating that F is stronger than updraft E. F is also characterized by anomalously low ρ_{HV} and Z_{DR} around ~4.1 - ~4.6 dB on the western flank of this region (not shown). At 22:42:04 UTC, a new region of low-level cyclonic shear has developed in the hook region, and updraft E is less vigorous than at

22:40:02 UTC. A much smaller WER is located near the surface, indicating that the amount of falling precipitation has increased.

4.3. Z_{DR} Column and K_{DP} Column

The height of the Z_{DR} column is a useful indicator of the height of the updraft perturbed melting layer, as the column can extend several kilometers above the in-cloud melting layer outside of the updraft region. This region is dominated by a small concentration of large raindrops (> 2 mm), a few-water coated hailstones, and low concentration of small-drops as confirmed by aircraft penetrations in Brandes et al. (1995) and Loney et al. (2002). At the periphery of the updraft where the magnitude of the vertical velocity diminishes, the largest raindrops and coated hailstones begin to fall, enhancing Z_{DR} (Kumjian and Ryzhkov 2008). This coincides with findings of Conway and Zrnic (1993) and Loney et al. (2002). K_{DP} columns, however, are generally offset from Z_{DR} columns in supercells due to environmental wind shear (Hubbert et al. 1998; Loney et al. 2002; Kumjian et al. 2008). K_{DP} columns have been found to be associated with a high concentration of liquid water, i.e. raindrops, wet graupel, or liquid coated hail (Loney et al. 2002).

Vertical cross-sections taken between 22:16:09 UTC and 22:20:24 UTC indicate a tall Z_{DR} column on the north flank of updraft A. Figure 8 illustrates the height and intensity of the column with time.
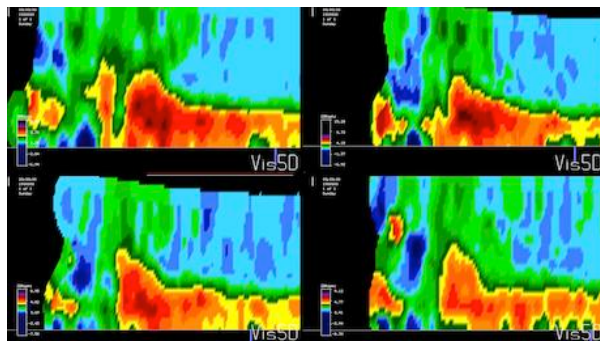

Figure 8 – Z_{DR} column on the northern flank of updraft A (seen in Figure 3). Vertical cross sections are taken at 22:16:09 UTC (top left), 22:17:37 UTC (top right), 22:18:55 UTC (bottom right), and 22:20:24 UTC (bottom right). Z_{DR} columns extend above the in-cloud melting layer (seen to the east (right) of the column) as much as several kilometers. The top of the volume is around ~6.0 km in these locations for all RHIs.

At 22:16:09 UTC the column extends around the northern edge of updraft A in a cyclonically curved manner towards the hook likely due to horizontal advection as noted by the column to the east of the updraft. Values of Z_{DR} > 5.0 dB and < 6.5 dB are seen up to ~4.6 km in height. However, it appears that shortly after updraft C is first seen (22:18:55 UTC), that the values in A's column diminish as seen at 20:20:24 UTC.

The height of the Z_{DR} column stays relatively consistent between 22:17:37 to 22:18:55 UTC. Between 22:20:24 and 22:24:00 UTC, there is a more substantial decrease in the height and weakening of the Z_{DR} in the column. No traditional K_{DP} columns seem to exist in any location at this time other than the southern tip of the hook, where there is believed to a high liquid water content. This is likely due to the presence of significant δ occurring in a broad region flanking the Z_{DR} column. The column in the hook is shown in Figure 9 at 22:20:24 UTC. The column extends to the top of the volume (~6.0 km). Values often fluctuate in this region due precipitation advecting around the hook and changes in updraft pulses.
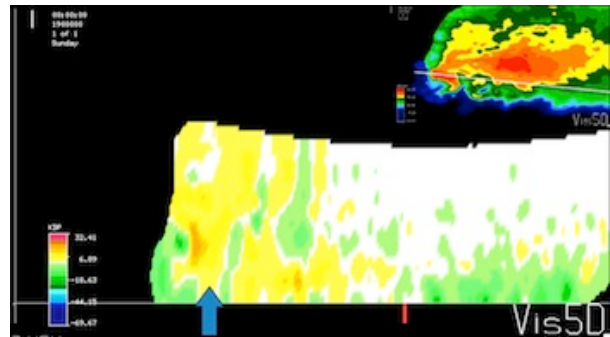

Figure 9 - Column of enhanced K_{DP} (denoted by blue arrow) in the hook region at 22:20:24 UTC. Inset is a Z_H CAPPI at 3.95 km denoting the location of the vertical slice. The height of volume at this location is ~6.0 km.

At 22:22:17 the remnants of the Z_{DR} column from updraft A are seen, but this region is now only ~0.50 km taller than the melting layer. Also a weak Z_{DR} column is located on the western periphery of updraft C at this time. This column occurs in a region of flanking weak echo associated with the rear-flank gust front. A weak slightly tilted Z_{DR} column flanks the north side of the mesocyclone from 22:22:17 to 22:24:05 UTC, and the tilt can be attributed to the strong cyclonic rotation advecting hydrometeors.
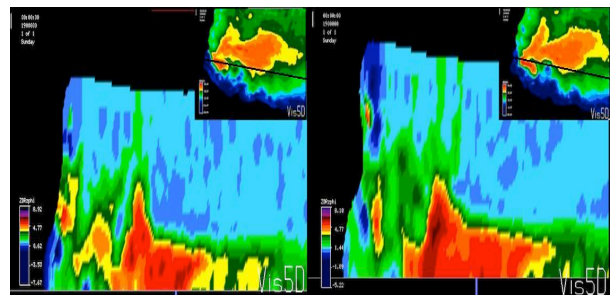

Figure 10 – Vertical cross sections of Z_{DR} columns from updraft's C and D at 22:26:04 UTC (left) and 22:28:04 UTC (right). The Z_H inset marks the location of the vertical cross section with respect to the updraft. Left inset taken at 4.01 km and right inset taken at 3.47 km. The height of the volume is up to ~7.0 km for both RHIs.

A well-defined Z_{DR} column has formed at 22:26:04 UTC with updraft C, which intensifies at the same time as updraft D. Values in the column are now ~6.5 dB as seen in Figure 10.

As shown in Figure 11 the column associated with updraft D is still present at 22:30:05 UTC (upper left). At 22:32:04, a new column has developed along the flanking region of the echo to the southeast of the previously mentioned column. This is associated with updraft E, and it should be noted that the column associated with updraft D (not shown) has diminished in height at this time. A decrease from ~6.5 dB to around 5.0 dB occurs between 22:35:47 UTC to 22:37:47 UTC.
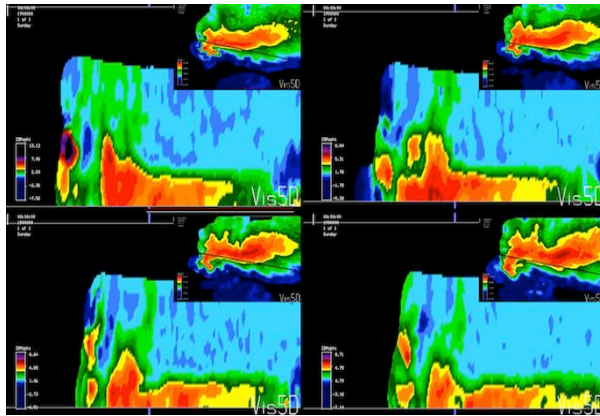
Figure 11 - Vertical cross sections illustrating the Z_{DR} column from 22:30:05 UTC (top left), 22:32:04 UTC (top right), 22:34:04 UTC (bottom left), and 22:36:04 UTC (bottom right). Insets of Z_H mark locations of slice at 1.50 km (top left), 0.96 km (top right), 0.51 km (bottom left), and 0.45 km (bottom right). Regions on the left flank of enhanced Z_{DR} are biased due to low SNR from attenuation. The height of the volume in these locations are ~7.0 km.

This column persists through the end of data collection, but there is also a column that develops in the increasing precipitation associated with the gust front. This occurs on the western edge of updraft E and the newly formed updraft F at 22:38:04 UTC. There is also some weak echo (Z_H is ~15 - ~25 dBZ) development on the inflow side of the forward flank that develops at ~22:33:46 UTC at ~5.73 km (top of the volume), and descends toward the surface by 22:36:16 UTC. The region at the surface does not intensify until 22:40:16 UTC. 22:37:15 UTC is the first time high Z_{DR} values (~4.5 to ~6.0 dB) are seen on the northwest flank of this weak echo. This signifies the horizontal extent of the updraft perturbed melting layer from the sequence of multiple updrafts. This Z_{DR} column is likely populated with mostly sparse large raindrops, which could be deduced from the low Z_H of the echo. There is a column of enhanced K_{DP} that develops in and around the BWER associated with updraft E at 22:36:04 UTC. This is shown in Figure 12. The large values aloft diminish after this time, but the two "column" regions in the hook and the weak echo development remains through the rest of data collection.
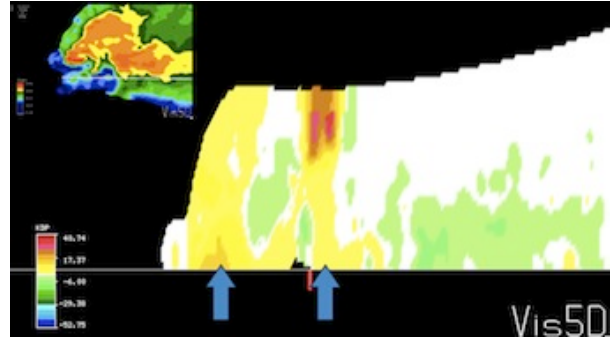

Figure 12 – K_{DP} vertical cross section at 22:36:04 UTC indicating the "column" region in the hook and extending through the weak echo. The inset is a CAPPI of Z_H at 5.25 km, and the white line indicates the location of the vertical slice. The blue arrows indicate the presence of the column in the hook (left arrow), and in the weak echo (right arrow). The height of the top of the volumes is ~6.0 km.

4.4. *Hail Signature*

Prior to the start of NOXP data collection, an NSSL Mobile Mesonet (Probe) reported 6.99 cm (2.75 inch) hail just north of the hook at 22:12:34 UTC, which lasted more than 10 minutes. The exact location of this report is unknown because of data loss associated with the windshield being knocked out, thus knocking the vehicle out of commission for the rest of the deployment. NOXP data at 22:16:09 UTC (Fig. 13) shows a hail signature that spans between the middle of the forward flank core (FFC), the rear flank core (RFC) region, and the northern hook region. This signature is defined by a reduction in ρ_{HV} (generally from ~0.4 to ~0.85), variable Z_H (~37 to ~65 dBZ), and Z_{DR} values between ~0 - ~2.5 dB. The attenuation correction retrieves much of the FFC region, and shows that this signature extends through the heart of the highest Z_H regime.
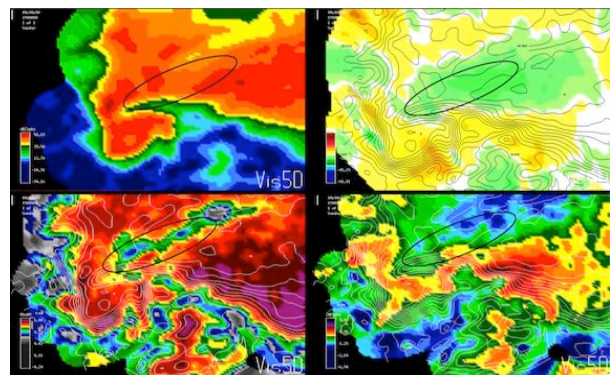

Figure 13 - CAPPI at 1.41 km of Z_H (top left), K_{DP} (top right), ρ_{HV} (bottom left), and Z_{DR} (bottom right) at 22:16:09 UTC. The ellipse outlines the narrow corridor where hail is located. Note the negative K_{DP}, low ρ_{HV}, moderate Z_H, and low Z_{DR} associated with larger hail.

Non-uniform beam filling has been ruled out behind these regions of heavy core, as this signature extends vertically to unattenuated regions. This region is instead

attributed to significant negative δ as noted in K_{DP} in Figure 13. Fluctuations of these values are thought to be associated with varying number concentration, varying diameters, and varying composition. Again care must be taken using Z_H, Z_{DR}, and ρ_{HV} due to significant attenuation that can yield low SNR bias issues.

As mentioned before, this reduction corridor is seen aloft, but it is also seen down low indicating vertical continuity as seen in the RHI at 22:16:09 UTC in Figure 14.
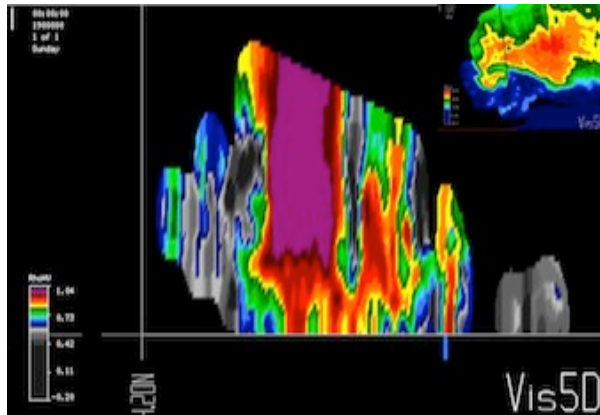

Figure 14 - RHI of ρ_{HV} illustrating the ρ_{HV} "corridor" signifying the reduction regime due to hail. Inset is a Z_H CAPPI taken at 0.42 km at the time of 22:16:09 UTC. The max height of the RHI is ~7.65 km.

Between 22:18:50 and 22:21:37 UTC, ρ_{HV} values have decreased from previous observations. This could be associated with the descent of hail produced from updraft A, and updraft B. At 22:17:15 UTC Probe 3 reported 4.45 cm (1.75 inch) hail falling just north of the hook on the southern end of the RFC region. Furthermore, values of Z_{DR} at different heights drop to < 0.4. However, no pattern was found in the heights of these anomalously low values as the 22:18:55 UTC observation is at 1.44 km in height, and at 22:20:24 UTC the height observation is up to 1.81 km. Perhaps the onset of updraft C at 22:18:55 UTC provided additional support for continued growth and more stones are falling at this time? It remains unclear as to the true value of ρ_{HV} that extends eastward into the attenuated northern FFC region. There is a possibility of smaller liquid coated hail and/or large raindrops in this region of the core, which is inferred from the amount of A_H and A_{DP} in this region.

Around 22:22:41 UTC Probe 7 reported 4.45 cm (1.75 inch) hail mixed with rain in the vicinity of the hail signature. At this time ρ_{HV} (~0.70 to ~0.75) in this vicinity, possibly due to the descent of hail. This region is believed to be associated with liquid coated hail due to the region of total attenuation identified in CAPPIs at 0.96 km at 22:26:04 and at ~1.60 km at 22:28:04 UTC (Figure 15). Above 1.58 km the easternmost ρ_{HV} reduction decreases in the 22:28:04 UTC volume. Z_H values in this core region are between ~55 - ~60 dBZ.

Z_{DR} values are ~1.0 - ~2.5 dB. Total attenuation is no longer seen at 2.54 km in height at the 22:28:04 UTC volume, and last seen at 2.71 km in the 22:26:04 UTC volume. Z_H and Z_{DR} values around this region are misleading, as the attenuation correction method cannot correct these regions. Therefore horizontal extent of these values and true magnitude of these values is unknown.
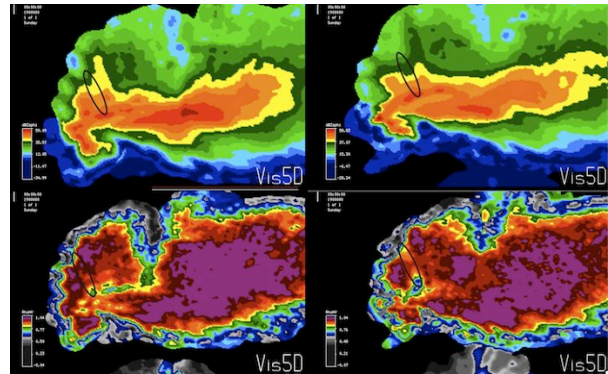

Figure 15 - Region of total attenuation in Z_H and ρ_{HV} indicated with the ellipses. The CAPPIs are at 22:26:04 UTC (left) and 22:28:04 UTC (right) at 0.96 km (left) and 1.61 km (right) in height.

At 22:30:05 UTC there is a substantial amount of total attenuation biasing the ρ_{HV} that is seen in both Z_H and the lack of ϕ_{DP} (not shown), which decreases with height. The total attenuation diminishes at 22:38:04 UTC. ρ_{HV} increases a bit and Z_H remains constant. At 22:40:05 UTC there are more regions down radial that are experiencing A_{DP} and A_H. This is likely due to the increased rainfall within the storm. After 22:39:47 UTC, the eastern extent of the ρ_{HV} reduction diminishes, but the reduction still extends west at 22:40:05 UTC.

The "V-notch" or "flying eagle" structure often seen in supercells has been thought to acquire its shape through the environmental flow diverting around the somewhat impenetrable updraft (e.g., Newton and Newton 1959; Fujita 1965; Fankhauser 1971; Brown 1992). Model results from Kumjian and Schenkamn (2008) reveal the flow is actually diverted by pressure perturbations, which are driven by wind shear around the updraft. Here, the characteristic shape is that of the flying eagle, and the ρ_{HV} reduction corridor correlates to the parent stormstructure extending back into the RFC. The ρ_{HV} values slightly increase with increasing height. For example, between 22:24:05 UTC and 22:26:04 UTC the supercell acquires a more significant V-notch structure as seen in Figure 16. CAPPIs at 4.77 km show Z_H increasing in the northwest flank of the RFC region, and ρ_{HV} decreasing at this time. Values around 4.77 km are between ~0.70 - ~0.73 and Z_{DR} is ~0 - ~1.0 dB. Between 22:26:04 UTC and 22:29:47 UTC ρ_{HV} begins decreasing further northeast as seen in Figure 16. At 22:38:04 UTC the northern extent of lower ρ_{HV} diminishes above 5.0 km in height.
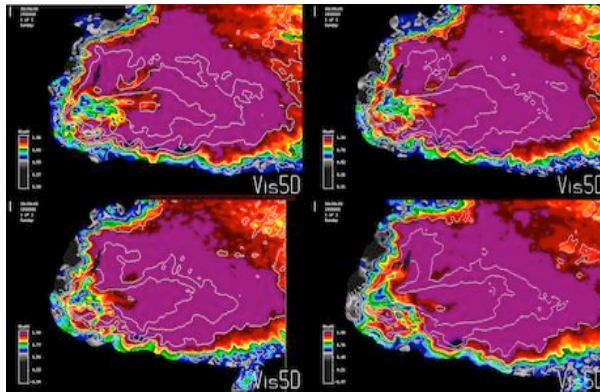
Figure 16 - CAPPIs taken at 4.77 km from 22:22:17 UTC to 22:28:04 UTC, which illustrate the evolution of the ρ_{HV} reduction corridor associated with advection of graupel and/or small hail on the northwest flank of the V-Notch. The black arrows denote the region of interest. Z_H is plotted every 10 dBZ (white contours), with larger values extending northeast in the left "wing" with time.

It is speculated that graupel and/or small hail advects off of the updraft northwestward in a region of stronger winds in the storm. This advection curves cyclonically north of the hook region, and then the faster environmental winds advect the lighter particles downstream (i.e. northeast along the northwest flank of the echo). Attenuation behind the hook increases with time thus care be must taken in this region. Whether this signature is ubiquitous to this structure is unknown, as it will take more cases to draw any conclusions.

4.5. Z_{DR} Arc Evolution

The Z_{DR} arc is known to be common to supercells around the world (e.g. Höller et al. 1994; Outinen and Teittinen 2007; Kumjian and Ryzhkov 2008; Kumjian 2008; Van Den Broeke 2008). This signature is found along a Z_H gradient on the inflow side of the storm below the melting level. Kumjian and Ryzhkov (2008, 2009) theorize that the Z_{DR} arc is a product of size sorting from impacts of Storm Relative Environmental Helicity (SREH; Davies Jones et al. 1990). There is a Z_{DR} arc defined by values up to ~6.5 dB initially at 22:16:22 UTC, which becomes more elongated by 22:17:37 UTC, and then begins to weaken at 22:18:55 UTC as seen in Figure 17. This weakening in the arc could be associated with updraft C lofting the sparse large hydrometeors believed to be present in the arc region (Kumjian and Ryzhkov 2008; Kumjian 2008). This could easily reduce the values in the arc region.

At 22:24:05 UTC there is no organized arc as seen in Figure 18, with the higher Z_{DR} values extending into the forward core region. Fig. 18 also illustrates the onset of updraft D at 22:26:04 UTC. Z_{DR} values increase in the southern region of the forward flank on the inflow side. This is seen spanning across a gradient of Z_H Also, the northern flank of Z_{DR} (note the two arrows in Figure 18, top right) divides into two "branches" in the

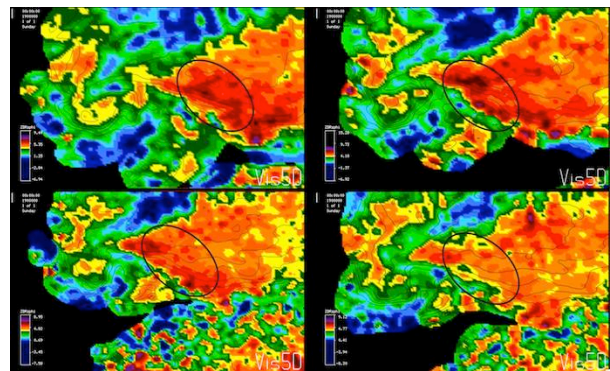FFC region. Shortly thereafter the two regions merge together as seen at 22:28:04 UTC.

Figure 17 – CAPPIs of Z_{DR} taken at 0.76 km that illustrate the evolution of the Z_{DR} arc from 22:16:22 UTC to 22:20:16 UTC. Note the weakening of the arc due to a new updraft forming.

The mechanism for this remains unclear, but perhaps this is related to the oscillations of the Z_{DR} arc and its relationship with the cycles of updrafts? More investigation is required.

At 22:28:04 UTC, the arc's values increase to around ~6.0 to ~6.5 dB on the flank of updraft C. The height of the arc region extends to 1.36 km, and is likely enhanced by the presence of the updrafts C and D on the western periphery of the arc. Size sorting due to vertical velocities should not be ruled out as a contributing factor to the distribution of the largest drops.
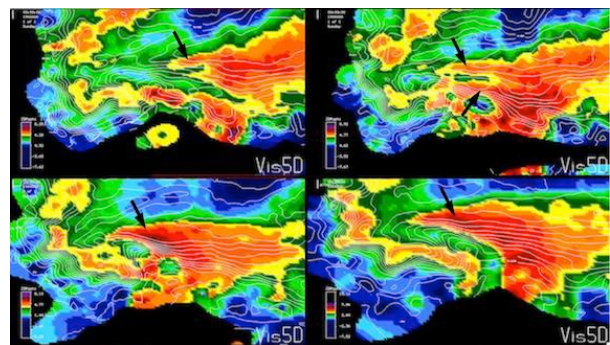

Figure 18 - CAPPIs at different heights illustrating the Z_{DR} arc evolution from 22:24:05 UTC (top left) at 0.79 km, 22:26:04 UTC (top right) at 0.73 km, 22:28:04 UTC (bottom left) at 1.36 km, and 22:30:05 UTC (bottom right) at 1.27 km. Black arrows denote the arc regions.

At 22:30:05 UTC the larger drops are distributed along the entire length of the inflow side of the echo. However, falling precipitation leads to rapid fluctuations that are under sampled in the two-minute time syncs.

By 22:32:04 UTC high Z_{DR} values have descended to near the surface in the arc region as values above 0.37 km diminish as seen in Figure 19. In the 22:34:17 UTC volume the arc has become disorganized and evolved into a "divided" appearance again.
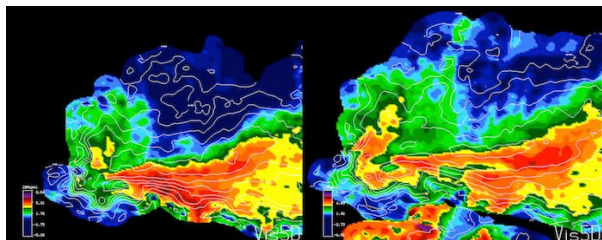
Figure 19 - CAPPIs illustrating the redistribution of the Z_{DR} arc taken from 22:32:04 UTC (left) at 0.37 km and from 22:34:04 UTC at 0.93 km. Z_H (white contours) is contoured every 5 dBZ.

This region of Z_{DR} is reduced, and it is speculated that environmental winds are advecting hydrometeors (both water and ice) that are now lofted by updraft E. This has a redistribution effect to the eastern edge of the forward flank (along the Z_H gradient), and is seen up to ~2.0 km in height. Below this height Z_{DR} increases, which indicates that hydrometeors are likely falling out. No Z_{DR} arc occurs in the remaining times of data collection. However, this does not rule out the possibility of reorganization following the increase in the low-level circulation at 22:42:04 UTC.

5. 7 JUNE 2009

On June 7, 2009 NOXP deployed twice on a supercell. The first deployment was east of Oregon, MO. The supercell was initially non-tornadic, but later produced a brief tornado during a second, shorter deployment.The radar began high-resolution scans at 23:42:07 UTC and ended at 00:03:48 UTC. The storm initially had a more classic look to it, but around ~23:48:00 UTC, the hook became very ragged as the storm transitioned to an outflow dominant high precipitation storm. It should be noted that the storm was in very close proximity to the radar, and this limited the height to which the radar was scanning. Local soundings indicate that the environmental melting layer is ~4.0 km above sea level, and the in-cloud melting layer is ~2.94 km above sea level.

5.1. *Updraft Signature*

There is a narrow updraft signature (updraft A) at 23:42:07 UTC along the inflow side of the hook region that extends into the hook. As seen in Figure 20, the updraft regime (identified with the blue arrow) shows a very narrow gradient between the updraft and the downdraft area. The substantial reduction of ρ_{HV} (down to ~0.68) is thought to be associated with a mixture of light debris and sparse large hail. Z_H in this location is around ~30 - ~35 dBZ, and Z_{DR} is around ~1.0 - ~1.5 dB.
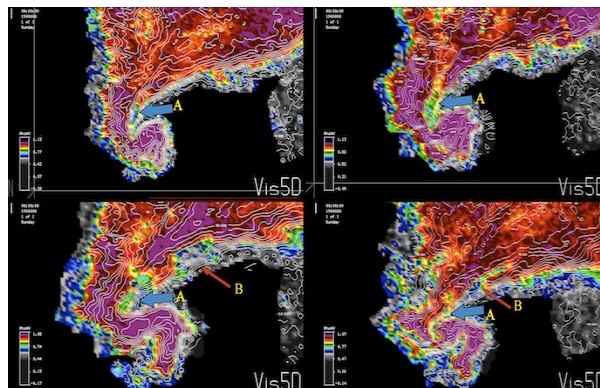

Figure 20 – CAPPIs of ρ_{HV} reduction regions in updraft locations (indicated by arrows) at 23:42:07 UTC at 0.65 km, 23:44:04 UTC (top right) at 0.11 km, 23:46:04 UTC (bottom left) at 0.59 km, and 23:48:05 UTC (bottom right) at 0.90 km. Overlaid are Z_H contours in white plotted every 5 dBZ.

The reduction region increases in value, and at 23:46:04 UTC a new updraft (updraft B) is seen northeast of A (identified with the red arrow). This region is marked by a reduction of ρ_{HV} less than 0.4, a low Z_H value of ~30 - ~35 dBZ, and Z_{DR} between ~0.5 - ~3.5 dB.

At 23:50:04 UTC there appears to be evidence of a new updraft (updraft C) seen in the polarimetric variables. Updraft C occurs further northeast along the forward flank core region as seen in Figure 21.
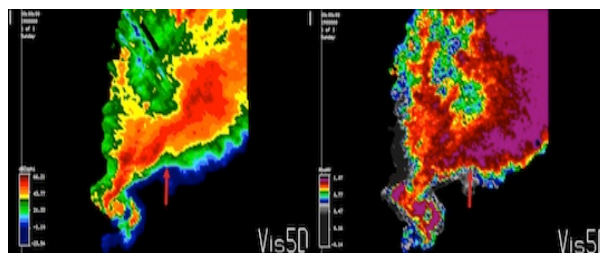

Figure 21 - CAPPIs of Z_H (left) and ρ_{HV} (right) at 23:50:04 UTC at 1.85 km in height.

Between 23:50:00 UTC and 23:56:00 UTC there is a descending reflectivity core (DRC) on the western flank of updraft C. This DRC is characterized by ~5 – ~45 dBZ (increasing values with increasing height), Z_{DR} values between ~5.0 - ~6.5 dB, with larger values lower in height, and ρ_{HV} values that increase with height (between ~0.73 and ~0.90). ρ_{HV} increases to ~0.99 by 23:56:04 UTC, and Z_{DR} increases to values between ~4.5 - ~7.0 dB. This is likely from larger hydrometeors descending off of the updraft from aloft. At 23:54:04 UTC, a new updraft region (updraft D) on the northeastern side of the DRC is seen in CAPPIs in Fig. 22.

In the 23:54:04 UTC volume, there is another intensified region of echo south of the previous DRC region. This reduction region (which is associated with hail) separates the Z_{DR} column above 2.50 km. Here ρ_{HV} reduces to low values only in region of what is believed
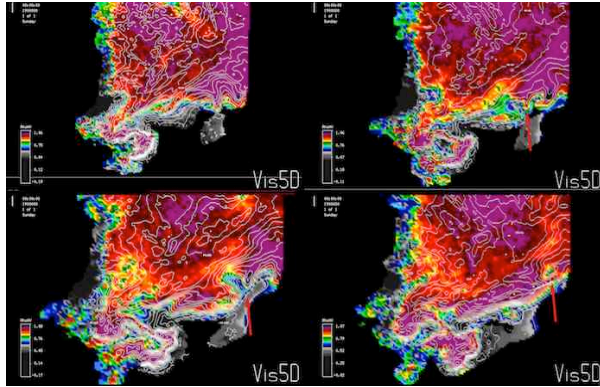
Figure 22 - CAPPIs taken at 1.43 km of ρ_{HV} with Z_H contoured (in white) every 5 dBZ. The times are 23:52:04 UTC (top left), 23:54:04 UTC (top right), 23:56:04 UTC (bottom left), and 23:58:04 UTC (bottom right). Updraft D is denoted with the red arrow.

to be low SNR. The values extending back into the core region increase inward from ~0.70 to ~0.90. ρ_{HV} values in regions of ~40 - ~45 dBZ are 0.80 +. There might be a concentration of hail and/or graupel here. At 23:58:04 UTC, this updraft region appears to be weakening as the diameter of the updraft is diminishing, and the region is becoming filled with precipitation. Hereafter the eastern extent of the echo moves out of the sector. The broad extent, proximity to the radar, and propagation makes any significant evidence of cyclic updrafts difficult to determine. The main reductions are likely attributed to hail, which will be discussed more thoroughly in section 5.3.

5.2. Z_{DR} Column and K_{DP} Column

At 23:42:07 UTC a broad Z_{DR} column is seen due north of updraft A, which extends up to at least 5.14 km in height. The column is significantly more narrow towards the top, and is defined by values between ~4.5 – ~6.5 dB (Figure 23). At 23:46:04 UTC the Z_{DR} column wraps from the north side to the eastern side of the
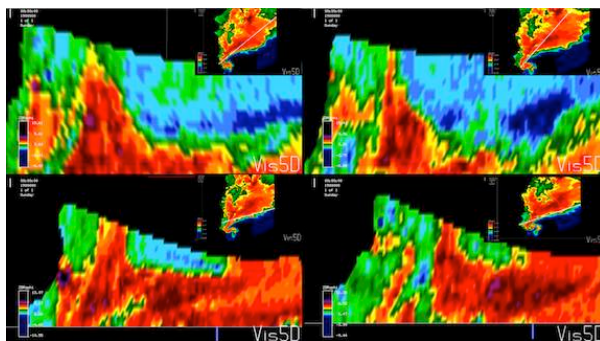

Figure 23 - Vertical slices indicating the Z_{DR} column adjacent to updraft A. Insets are CAPPIs of Z_H at 1.10 km indicate the location of the slices. Columns are at 23:42:07 UTC (top left), 23:44:04 UTC (top right), 23:46:04 UTC (bottom left), and 23:48:05 UTC (bottom right). The top of the volume is ~4.90 km in height.

updraft, which extends to the top of the volume (~4.75 km at this location). However, at 23:48:05 UTC, values in the column due north of the updraft, subside and the higher values shift to the region and due west of the developing updraft B. Values in the column range between 4.0 to 6.5 dB. However, the column quickly diminishes in magnitude between 23:50:04 UTC and 23:52:04 UTC. Values decrease to between 2.0 – 3.0 dB, with the higher values occurring in the center of the column.

Also seen between the time period of 23:42:07 UTC and 23:48:05 UTC is a column of K_{DP} in the hook echo indicating the presence of liquid hydrometeors. This is shown in Figure 24. The K_{DP} values are up to ~30° km^{-1} to ~45° km^{-1} in the backside of the hook region. This is a region biased by attenuation.
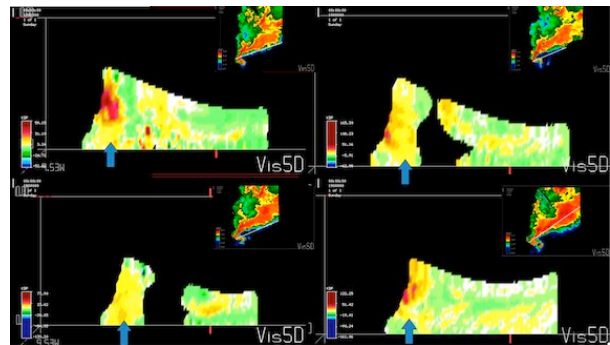

Figure 24 - Vertical slices indicating the "column" of K_{DP} at 23:42:07 UTC (top left), 23:44:04 UTC (top right), 23:46:04 UTC (bottom left), and 23:48:05 UTC (bottom right). Insets are Z_H CAPPIs at 2.50 km (top left) in height, 2.81 km (top right) in height, 2.25 km (bottom left) in height, and 1.88 km (bottom right) in height. The top of the volume is ~4.90 km in height.

After 22:48:25 UTC there is a very narrow column to the east of the old column's location and to the west of a DRC region (not shown), with values between 4.0 to 6.5 dB. It should be noted that very high Z_{DR} values (between ~3.5 - ~5.5 dB) extend across the entire forward flank of the supercell to the top of the resolution volume, but the close proximity of the storm limits vertical resolution. This includes everywhere along the forward flank region at 23:58:04 UTC to 00:02:04 UTC. Therefore, it is unclear to what height the high Z_{DR} values extend up to. It is expected that the tallest Z_{DR} regions are located along the periphery of the updraft regions.

5.3. Hail Signature

As mentioned before and seen in Figure 20, the region flanking the updraft A is characterized by low Z_{DR} (~0.5 to ~1.0 dB), ρ_{HV} down to ~0.59 to ~0.75, and ~25 - ~34 dBZ. It is found on the inflow side of the hook region, and is very consistent with height. This signature is associated with hail fall. The sharp gradient between updraft and downdraft is seen in the dual-polarimetric

variables. The initial flanking region is a region of low number concentration of larger hail (i.e. the low Z_H region) falling on the periphery of the downdraft region in the hook. At 23:42:20 UTC the hail signature is seen on the southernmost point on the side of the inflow. A region of high Z_H (up to ~62 dBZ) flanks this region, where higher concentrations of hydrometeors are present and are believed to be liquid coated hail. UMass X-Pol reported tennis ball and golfball sized hail in this region at 22:44 UTC, which persisted for at least 10 minutes as the storm propagated eastward. Up to 2.02 km in height Z_H values, in the shank of the hook are up to ~62 dBZ. Significant attenuation occurs on the backside from the high number concentration.

Between 23:44:04 UTC and 23:46:05 UTC the amount of hail fall increases to the northeast as seen in Figure 25. CAPPIs taken at different heights indicate fluctuations in Z_{DR}. These fluctuations could be associated with updraft B lofting hail, or it could be horizontal or vertical displacement. Note the dividing of the Z_{DR} column on the northeast side at 23:44:04 UTC (Figure 25).
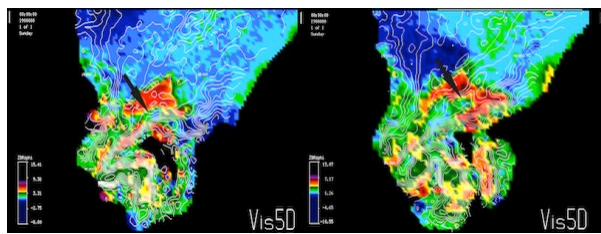

Figure 25 - Hail signature redistribution as seen in Z_{DR} in CAPPIs at 3.40 km in height at 23:44:04 UTC (left) and 23:46:05 UTC (right). Z_H is overlaid in white contours every 5 dBZ. The black arrows indicate the location of the hail regime.

Between 23:44:04 UTC and 23:46:05 UTC the hail corridor descends toward the surface as indicated by the reduction in ρ_{HV} and Z_{DR} near the surface at 23:46:05 UTC. At 23:48:05 UTC Z_H increases in the low-level regions of the hook, which indicates the increase in hail descent. ρ_{HV} in these regions is around ~0.81 to ~0.84. At 23:50:04 UTC through 23:56:04 UTC, the size and/or number concentration of hail is increasing as ρ_{HV} is dropping in the hook region (ranging from ~0.90 to ~0.75) at 0.31 km and all along the forward flank region as seen in Figure 26. UMass X-Pol reported ~10.16 cm (4.0 inch) hail at 23:50 UTC in this location. At 23:54:04 UTC ρ_{HV} begins to decrease along the inflow side of the forward flank region, and at 23:56:04 UTC there is a substantial decrease in ρ_{HV} (~0.70 to ~0.75). Z_{DR} also drops in the forward flank region to (~1.0 to ~2.5 dB), and occurs in a region of Z_H between 35 and 40 dBZ.

As shown in Fig. 26 at 23:56:04 UTC, updraft C is seen to be producing a significant amount of hail This "hail corridor" occurs on the leading edge of the forward flank region of the echo. ρ_{HV} along this region begins to
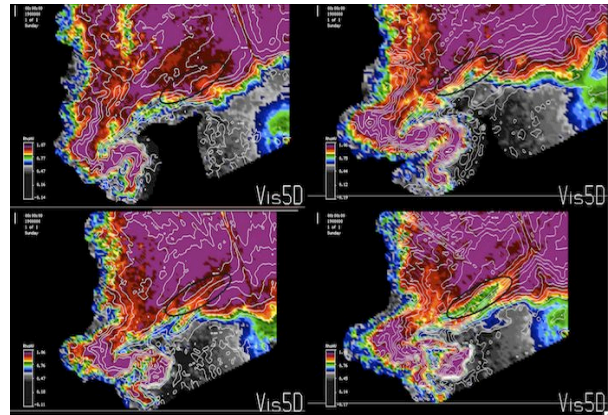

Figure 26 - CAPPIs taken at 0.31 km in height of ρ_{HV}. Reductions in values indicate a substantial increase in hail fall between 23:50:04 UTC (top left), 23:52:04 UTC (top right), 23:54:04 UTC (bottom left), and 23:56:04 UTC (bottom right). Overlaid are white contours of Z_H every 5 dBZ.

increase above 3.08 km. The DRC region (not shown) looks like small hail down low and pure graupel higher up as Z_H is between 30 – 35 dBZ, Z_{DR} is around 1.0 to 2.0 dB, and ρ_{HV} is between 0.55 – 0.60 at 0.51 km in height. Between 23:58:04 UTC and 00:02:04 UTC, the narrow Z_{DR} and ρ_{HV} reduction regions move farther east. This is due to the propagation of the storm. This regime is characterized by Z_{DR} ~0.55 to ~2.0 dB, and ρ_{HV} between ~0.70 to ~0.88 at 23:58:04 UTC and further weakens by 00:00:04 UTC as seen in CAPPIs at 0.20 km in Figure 27. This region moved out of the sector by 00:02:04 UTC.
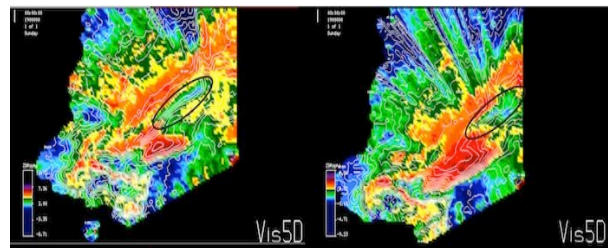

Figure 27 - CAPPIs at 0.20 km of Z_{DR} at 23:58:04 UTC (left), and at 00:00:04 UTC (right) with ellipses indicating the "hail corridor". White contours are of Z_H at every 5 dBZ.

Around the melting layer there is sharp gradient seen in ϕ_{DP} immediately behind the corridor of higher Z_{DR} values as seen in Figure 28. This signature is seen most significantly during the earlier scans since storm propagation limited the height of observations later on. This signature is similar to the melting layer signature as noted in Melnikov et al. (2005). This region is attributed to significant backscatter differential phase and is believed to be from large liquid coated hail, but concentrated on the back edge of the Z_{DR} corridor and the Z_H core. It remains unclear as to the number concentration and the distribution of these larger particles. Beyond this sharp reduction region, the

differential phase does not increase with distance, which diminishes attenuation correction. It is important to note that A_H and A_{DP} is still occurring through the heavy core preceding this region. However, Z_H and Z_{DR} beyond this region remain lower than expected as seen in Figure 28. The logical explanation would be that this region is dominated by small graupel, ice crystals, or other frozen particles as there are still higher Z_H values beyond this region above the melting layer.

5.4. Z_{DR} Arc Evolution

The Z_{DR} arc that has been noted in literature does not appear throughout this data collection period. However, there is a very broad region of high Z_{DR} values that spans the entire forward flank region along the inflow side of the echo (not shown). Though this region still occurs along a gradient in Z_H, attenuation prevents the true horizontal extent of these values from being determined. At lower elevations the higher Z_{DR} values extend back into the core regions, indicating the presence of large number concentrations and large drops. Near the top of the volume (~3.50 km at 23:42:07 UTC, and decreasing to ~2.30 km at 00:02:04 UTC) the higher Z_{DR} values are generally confined to the region along the easternmost extent of the echo, this region is at or below the melting layer.
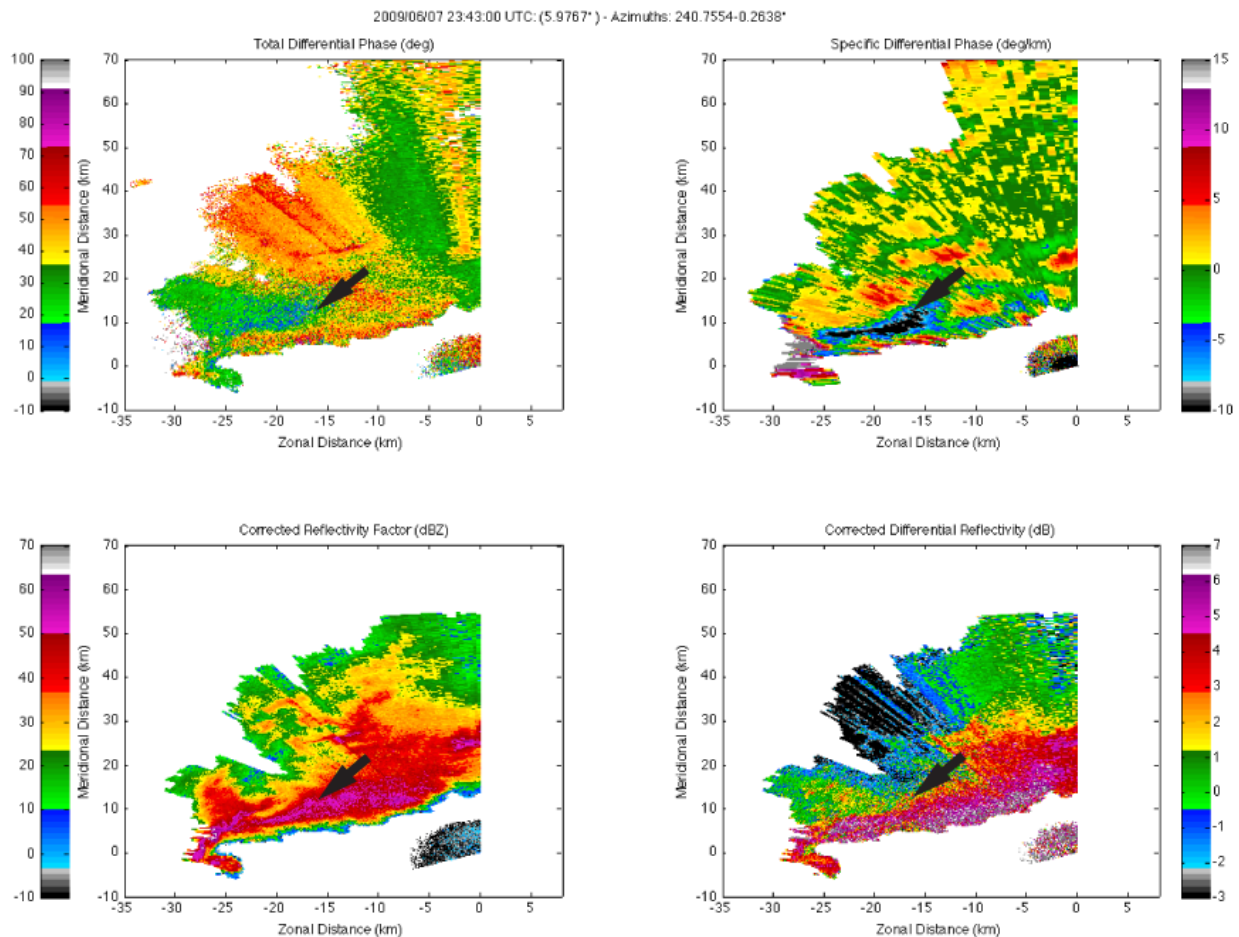

Figure 28 - 4-panel of PPIs at 6.0 degrees elevation at 23:43:00 UTC of ϕ_{DP} (top left), K_{DP} (top right), attenuation corrected Z_H (bottom left), and attenuation corrected Z_{DR} (bottom right). Note the significant amount of δ (denoted by the black arrows) occurring on the back edge of the core region. This is seen around the melting layer, and is believed to be a narrow region of liquid coated hailstones. Also note the biases in the attenuation correction as a result of this.

6. SUMMARY

Data collected by NOXP on two supercells have been examined. Both data sets are processed with an attenuation correction technique called the ZPHI Rain-Profiling Algorithm. One of the supercells was strongly tornadic (June 5), and one of which was weakly tornadic (June 7). Both storms produced large hail, but June 5 progressed as a more classic supercell with diminishing hail size as time elapsed, and June 7 evolved into an outflow dominant high precipitation supercell. A tornadic vortex signature (TVS) is seen in the early stages of June 5, but limitations, such as the dropout of ρ_{HV} in the vicinity of the tornado's location, and the wide gate width limit the capability of seeing this signature. Cyclic evolution of the updraft is seen in Z_H often between ~25 – ~30 dBZ, Z_{DR} between ~ -0.6 to ~1.5 dB, and ρ_{HV} ranging from ~0.25 to ~0.85. These values do vary some in time, but are characteristic of the type of scatterer in the updraft.

A unique hail signature is seen with variable Z_H often between ~30 - ~65 dBZ, low Z_{DR} between ~0 dB to ~2.5 dB, and ρ_{HV} ranging from ~0.25 to ~0.85 in both the June 5 and June 7 cases. Number concentration, hydrometeor type, and diameters are seen to impact these values in both storms. In both storms, there appears to be a "hail corridor" region, but is found in different locations for each storm. June 5's "hail corridor" is located just north of the hook echo, and extends well into the forward flank region. Furthermore, the distance from the echo allowed the radar to observe this "corridor" to assume the shape of the parent "V-notch" or "flying eagle" structure. The evolution of this signature is seen over a period of 2 to 4 minutes. It occurs at different heights in the storm as a result of redistribution of hydrometeors due to environmental and the storm's winds. June 7's "hail corridor" region is found just on the inflow side of the shank of the hook, and later on along the leading edge of the forward flank region.

Z_{DR} columns are seen to rapidly correlate to the onset of a new updraft. Values in the column are seen up to 6.5 dB. However, in both storms K_{DP} columns are most commonly seen in the location of the hook echo. This could be biased by the amount of backscatter differential phase δ present in the forward flank regions masking the K_{DP} columns there. The height to which the column extended on June 7 is undetermined because of the close proximity of the radar to the echo, and a lower height of the highest elevation angle of data collected. A well-defined Z_{DR} arc is found in the June 5 case, which oscillates throughout the time period of new updraft pulses. The arc region diminishes towards the end of data collection. No Z_{DR} arc is seen for the June 7, 2009 case.

7. ACKNOWLEDGEMENTS

8. REFERENCES

Barnes, S.L., 1964: A technique for maximizing details in numerical weather map analysis. *J. Appl. Meteor.*, **3,** 396-409.

Brandes, E.A., J. Vivekanandan, J.D. Tuttle, and C.J. Kessinger, 1995: A study of thunderstorm microphysics with multiparameter radar and aircraft observations. *Mon. Wea. Rev.*, **123,** 3129-3143.

Bringi, V.N., and Chandrasekar, 2001: *Polarimetric Droppler Weather Radar: Principles and Applications.* Cambridge University Press, 636 pp.

Bringi, V.N., T.D. Keenan, and V. Chandrasekar, 2001: Correcting C-band radar reflectivity and differential reflectivity data for rain attenuation: A self-consistent method with constraints. *IEEE Trans. Geosci. Remote Sens.*, **39,** 1906-1915.

Bringi, V.N., V. Chandrasekar, N. Balakrishnan, and D.S. Zrnic, 1990: An examination of propagation effects in rainfall on radar measurements at microwave frequencies. *J. Atmos. Oceanic Technol.*, **7,** 829-840.

Brown, R. A., 1992: Initiation and evolution of updraft rotation within an incipient supercell thunderstorm. *J. Atmos. Sci.*, **49,** 1997-2014.

Caylor, I., and A.J. Illingworth, 1987: Radar observations and modeling of warn rain initiation. *Quart. J. Roy. Meteor. Soc.,* **113,** 1171-1191.

Conway, J.W., and D.S. Zrnic, 1993: A study of embryo production and hail growth using dual-Doppler and multiparameter radars. *Mon. Wea. Rev.*, **121,** 2511-2528.

Davies-Jones, R. D.W. Burgess, and M. Foster, 1990: Test of helicity as a forecast parameter. Preprints, *16th Conf. on Severe Local Storms*, Kananaskis Park, Alberta, Canada, Amer. Meteor. Soc., 588-592.

Doviak, R.J., and D.S. Zrnic, 1993: *Doppler Radar and Weather Observations.* Academic Press, 562 pp.

Fankhauser, J. C., 1971: Thunderstorm environment interactions determined from aircraft and radar observations. *Mon. Wea. Rev.* , **99,** 171-192.

Fujita, T., 1965: Formation and steering mechanisms of tornado cyclones and associated hook echoes. *Mon. Wea. Rev.*, **93,** 67-78.

Heinselman, P.L., and A.V. Ryzhkov, 2006: Validation of polarimetric hail detection. *Weather and Forecasting*, **21,** 839-850.
Hitschfeld, W., and J. Bordan, 1954L Errors inherent in the radar measurement of rainfall at attenuation wavelengths. *J. Atmos. Sci.,* **11,** 58-67.

Höller, H., V.N. Bringi, J. Hubbert, M. Hagen, and P.F. Meischner, 1994: Life cycle and precipitation formation in a hybrid-type hailstorm revealed by polarimetric and Doppler radar measurements. *J. Atmos. Sci.*, **51,** 2500-2522.

Hubbert, J., and V.N. Bringi, 1995: An iterative filtering technique for the analysis of the copolar differential phase and dual-frequency radar measurements. *J. Atmos. Oceanic Technol.*, **12,** 643-648.

Hubbert, J., V.N. Bringi, L.D. Carey, and S. Bolen, 1998: CSU-CHILL polarimetric measurements from a severe hailstorm in eastern Colorado. *J. Appl. Meteor.*, **37,** 749-755.

Illingworth, A.J., J.W.F. Goddard, and S.M. Cherry, 1987: Polarization radar studies of precipitation development in convective storms. *Quart. J. Roy. Meteor. Soc.,* **113,** 469-489.
Jameson, A.R., 1991: Polarization radar measurements in rain at 5 and 9 GHz. *J. Appl. Meteor.*, **30,** 1500-1513.

Jameson, A.R., 1992: The effect of temperature on attenuation-correction schemes in rain using polarization propagation differential phase shift. *J. Appl. Meteor.*, **31,** 1106-1118.

Kennedy, P.C., S.A. Rutledge, W.A. Petersen, and V.N. Bringi, 2001: Polarimetric radar observations of hail formation. *J. Appl. Meteor.*, **40,** 1347-1366.

Koch, S.E., M. desJardins and P.J. Kocin, 1981: The GEMPAK Barnes objective analysis scheme. NASA Tech. Memo. ERL NSSL-51

Kumjian, M.R., 2008: Polarimetric radar analysis of microphysical processes in supercell storms. M.S. Thesis, University of Oklahoma, 188 pp. [Available from School of Meteorology, University of Oklahoma, 120 David L. Boren Blvd., Norman, OK 73072]

Kumjian, M.R., and A. V. Ryzhkov, 2008: Polarimetric

signatures in supercell thunderstorms. *J. Appl. Meteor. and Climatology*, **48,** 1940-1961.

Kumjian, M.R., and A. V. Ryzhkov, 2009: Storm relative helicity revealed from polarimetric radar measurements. *J. Atmos. Sci.,* **66,** 667-685.

Kumjian, M.R., and A.D. Schenkmean, 2008: Interpretation of the "flying eagle" radar signature in supercells. Extended Abstracts, *24th Conf. on Severe Local Storms*, Savannah, GA, Amer. Meteor. Soc., P14.2. [Available online at http://ams.confex.com/ams/pdfpapers/141917.pdf]

Loney, M.L., D.S. Zrnic, J.M. Straka, and A.V. Ryzhkov, 2002: Enhanced polarimetric radar signatures above the melting layer in a supercell storm. *J. Appl. Meteor.*, **41,** 1179-1194.

Majcen, M., P. Markowski, Y. Richardson, D. Dowell, and J. Wurman, 2008: Multipass objective analyses of Doppler radar data. *J. Atmos. Oceanic Technol.,***25,** 1845-1858.

Matrosov, S.Y., K.A. Clark, B.E. Martner, and A.Tokay, 2002: X-band polarimetric radar measurements on rainfall. *J. Appl. Meteor.* , **41,** 941-952.

Meischner, P.F., V.N. Bringi, D. Heimann, and H. Höller, 1991: A squall line in southern GermanyL Kinematics and precipitation formation as deduced by advanced polarimetric and Doppler radar measurements, *Mon. Wea. Rev.,* **119,** 678-701.

Melnikov, A.V., V.M. Melnikov, and A.V. Ryzhkov, 2005: On the differential phase in the melting layer. Extended Abstracts, *32nd Conference on Radar Meteorology/11th Conference on Mesoscale Processes*, Albuquerque, NM, Amer. Meteor. Soc., P9R.9.

Newton, C.W., and H. R. Newton, 1959: Dynamical interactions between latge convective clouds and environmental vertical shear. *J. Meteor.*, **16,** 483-496.
Outinen, K. and J. Teittinen, 2007: Case study of a tornadic supercell in Finland 28 August 2005. *Proc. Fourth European Conf. on Severe Storms,* Trieste, Italy, International Centre for Theoretical Physics, 05.14.

Oye, R., C.K.Mueller, and S. Smith, 1995: Software for radar translation, visualization, editing, and interpolation. Preprints, *27th Conference on Radar Meteorology*, Vail, CO, American Meteorological Society, 359-361.

Park, S.G., V.N. Bringi, V. Chandrasekar, M. Maki, and K. Iwanami, 2005: Correction of radar reflectivity and differential reflectivity for rain attenuation at X band. Part I: Theoretical and empirical basis. *J. Atmos. Oceanic Technol.*, **22,** 1621-1632.

Romine, G.S., D.W. Burgess, and R.B. Wilhelmson, 2008: A dual-polarization-radar-based assessment of the 8 May 2003 Oklahoma City area tornadic supercell. *Mon. Wea. Rev.,* **136,** 2849-2870.

Ryzhkov, A.V., D. Burgess, D. Zrnic, T. Smith, and S. Giangrande, 2002: Polarimetric analysis of a 3 May 1999 tornado. Preprints, *22nd Conf. onSevere Local Storms*, Hyannis, MA, Amer. Meteor. Soc., 14.2. [Available online at http://ams.confex.com/ams/pdfpapers/95684.pdf]

Ryzhkov, A.V., T. J. Schuur, D. W. Burgess, and D. S. Zrnic, 2005: Polarimetric tornado detection. *J. Appl. Meteor.*, **44,** 557-570.

Ryzhkov, A.V., and D.S. Zrnic, 1995: Precipitation and attenuation measurements at a 10-cm wavelength. *J. Appl. Meteor.*, **34,** 2121-2134.

Ryzhhkov, A.V., and D.S. Zrnic, 2005: Radar polarimetry at S, C, and X bands. Comparitive analysis and operational implications. Extended Abstracts, *32nd Conf. on Radar Meteorology*, Albequerque, NM, Amer. Meteor. Soc., 9R.3.

Snyder, J.C., 2008: Attenuation correction techniques and hydrometeor classification of high-resolution, X-band, dual-polarized mobile radar data of sever convective storms. M.S. Thesis, University of Oklahoma, 148 pp. [Available from School of Meteorology, Unviersity of Oklahoma, 120 David L. Boren Blvd., Norman, OK 73072].

Testud, J., E.Le Bouar, E. Obligis, and M. Ali-Mehenni, 2000: The rain profiling algorithm applied to polarimetric weather radar. *J. Atmos. Oceanic Technol.*, **17,** 332-356.

Tuttle, J.D., V.N. Bringi, H.D. Orville, and F.J. Kopp, 1989: Multiparameter radar study of a microburst: Comparison with model results. *J. Atmos. Sci.*, **46,** 601-620.

Van Den Broeke, M.S., J.M. Straka, and E.N. Rasmussenm 2008: Polarimetric radar observations at low levels during tornado life cycles in a small sample of classic Southern Plains supercells. *J. Appl. Meteor. Climatol.*, **47,** 1232-1247.

Zhang, G., 2008: *Personal communication*

Zrnic, D. S., and A. V. Ryzhkov, 1999: Polarimetry for weather surveillance radars. *Bull. Amer. Meteor. Soc.,* **80,** 389-406.